Energy & Environmental Science

ROYAL SOCIETY OF CHEMISTRY

PAPER

View Article Online
View Journal | View Issue

Cite this: *Energy Environ. Sci.*, 2024, **17**, 6279

High-throughput design of complex oxides as isothermal, redox-activated CO_2 sorbents for green hydrogen generation†

Runxia Cai,‡[a] Kunran Yang,‡[a] Xijun Wang,‡[ab] Mahe Rukh,[a] Azin Saberi Bosari,[a] Eric Giavedoni,[a] Alexandra Pierce,[a] Leo Brody,[a] Wentao Tang,[a] Phillip R. Westmoreland[a] and Fanxing Li*[a]

Received 16th May 2024,
Accepted 24th July 2024

DOI: 10.1039/d4ee02119c

rsc.li/ees

Sorption-enhanced reforming and gasification (SERG) offers a promising approach to intensify hydrogen production from carbonaceous feedstocks. However, conventional sorbents require substantial temperature increases for the endothermic CO_2 release step and are prone to deactivation. This study introduces a new class of redox-activated sorbents capable of stable isothermal operation and tunable heats of reactions, thereby facilitating an efficient reactive separation scheme. Using plane-wave density functional theory (DFT) calculations of structures and free energies, we screened 1225 perovskite-structured sorbent candidates, followed with extensive experimental validation. An effective descriptor, (ΔG_{abs} + ΔG_{reg}), was identified to expedite sorbent optimization. The advanced sorbents showed reversible, isothermal carbonation of up to 78% of the A-site cation, permitting isothermal SERG or "iSERG". Their versatility was demonstrated in a fluidized bed for woody biomass gasification and a packed bed for biogas conversion, yielding hydrogen-enriched (73 vol%) syngas from biomass and 95+% pure H_2 from biogas. Our results also support integrated CO_2 capture to produce carbon-negative hydrogen products.

Broader context

Hydrogen is a clean energy carrier with significant potential to advance global efforts towards carbon neutrality. Among the various production methods, green hydrogen generated from sorption-enhanced reforming and gasification (SERG) of biogenic feedstocks stands out as a promising approach. However, conventional SERG technologies face critical challenges, including sorbent deactivation, substantial temperature fluctuations, and the requirement for large energy inputs to facilitate CO_2 release. This study rationally designs and validates a unique family of redox-activated sorbents that are capable for isothermal CO_2 capture and release with excellent efficiency and stability for woody biomass and biogas conversion. Furthermore, they facilitate *in situ* CO_2 capture, leading to efficient hydrogen production with negative life cycle carbon emissions. Through integration with conventional Fischer–Tropsch and methanol synthesis technologies, the isothermal SERG technology can be extended to produce carbon negative methanol and liquid fuel. Our results represent a significant advancement in sustainable hydrogen production, paving the way for broader adoption and impactful carbon reduction.

1. Introduction

Hydrogen is widely recognized as a clean-energy vector that could contribute substantially to the global effort to achieve carbon neutrality.[1–3] However, less than 1% of the 94 million tons of hydrogen produced in 2021 was derived from non-fossil fuel sources.[4,5] Given the pressing need to address global climate change and the expected growth in hydrogen demand, it is highly desirable to develop new technologies that can produce carbon-free, cost-competitive hydrogen from renewable sources.[6,7] Biogenic feedstocks, such as biomass and biogas, represent abundant and sustainable alternatives to coal and natural gas for hydrogen production.[8–13] Nevertheless, conventional gasification and reforming processes are energy-intensive, and the distributed nature of biomass and biogas sources significantly hinders the ability to leverage economies of scale. Additionally, the compositional complexity of biogenic feedstocks further inflates system complexity and costs.[14–16]

[a] *Department of Chemical and Biomolecular Engineering, North Carolina State University, 911 Partners Way, Raleigh, North Carolina 27695-7905, USA. E-mail: fli5@ncsu.edu*
[b] *Department of Chemical and Biological Engineering, Northwestern University, Evanston, Illinois 60208, USA*

† Electronic supplementary information (ESI) available. See DOI: https://doi.org/10.1039/d4ee02119c

‡ These authors contributed equally to this work.

Consequently, the development of innovative technologies that markedly intensify the hydrogen production process is essential for achieving cost-competitive renewable hydrogen generation.

Sorption-enhanced reforming and gasification (SERG) represents a promising approach to simplify hydrogen production from biogenic resources. This objective is achieved by integrating gasification/reforming, the water–gas-shift reaction, and CO_2 capture into a single cyclic operation. This two-step operation comprises a reforming/gasification step (with *in situ* CO_2 capture) for H_2-rich syngas production, followed by a decarbonation step for sorbent regeneration.[17–20]

Practical implementation of SERG, however, is challenged by substantial energy consumption for the decarbonation step and lack of sorbent stability over repeated cycles. Notably, all high-temperature CO_2 sorbents reported in the literature to date require a large temperature swing ($\geq$100 °C) to drive the highly endothermic CO_2 release reaction (ΔH = 167.6 kJ mol^{-1} for $CaCO_3$ at 800 °C), a crucial condition for effective sorbent regeneration for practical applications.[21,22] However, such temperature swing operations incur considerable exergy loss and thermal stress on the particles and reactors. Moreover, the prevailing CaO-based sorbents typically lose 50–80% of their initial CO_2 sorption capacity after just a few dozen cycles.[23–26] While steam re-activation at a lower temperature proves effective in regenerating the CaO sorbents, it introduces additional process complexity and cost.[27]

Advanced sorbents with engineered structures have also shown promise by exhibiting significantly lower deactivation rates.[28–35] Nonetheless, the high cost of manufacturing these sorbents hinders their practical application, and the loss of activity, albeit slow, is generally irreversible without an additional reactivation step. Mixed oxide sorbents such as $Ca_3Co_4O_9$ and $Sr_{1-x}Ca_xFe_{1-y}Ni_yO_{3-\delta}$ have been explored in the context of sorption-enhanced steam reforming of glycerol. While these sorbents exhibit excellent cyclic stability through reversible phase transitions,[36–39] large temperature swings are still required for the decarbonization step. Our recent study indicated that perovskite sorbents such as $Sr_{0.25}Ba_{0.75}Fe_{0.375}Co_{0.625}O_{3-\delta}$ has the potential to operate isothermally for toluene reforming in the presence of a Ni-based reforming catalyst.[39] Nevertheless, ~100 °C temperature increase is still necessary for complete sorbent regeneration.

To address these challenges, this study proposes and systematically validates new families of redox-activated mixed-oxide sorbents capable of isothermal SERG (iSERG) operation with tunable heat of reaction and excellent cyclic stability. As depicted in Fig. 1, a redox-active, perovskite-structured ($ABO_{3-\delta}$) sorbent plays a central role in this two-step process. During the reforming or gasification step, the strongly reducing environment would trigger the reduction of the B-site metal cation (*e.g.*, $Fe^{3/4+}$), which induces phase segregation. As a result, the highly basic A-site cation (*e.g.*, Sr^{2+}) would bind with CO_2 to form carbonates. In the subsequent regeneration step, the carbonated and reduced sorbent is put in contact with air or O_2 to trigger the oxidation of the B-site metal, leading to

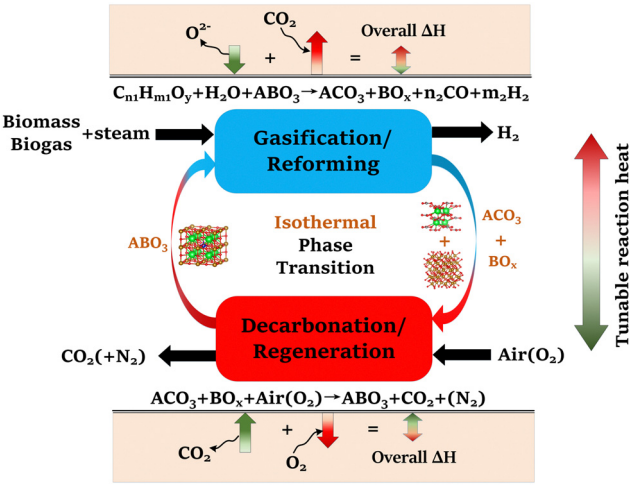

Fig. 1 Schematic of the isothermal sorption-enhanced reforming and gasification (iSERG) concept utilizing perovskite-structured isothermal sorbents.

spontaneous release of CO_2 and reformation of the $ABO_{3-\delta}$ structure. The variation in external oxygen chemical potentials would provide significantly higher thermodynamic driving force for carbonation and decarbonation reactions, when compared to temperature swings in conventional processes. Moreover, the heats for the reduction and oxidation reactions would counterbalance those of the exothermic carbonation and endothermic decarbonation reactions. Consequently, the considerable structural and compositional flexibility of perovskite oxides, as illustrated in this study, also opens a unique avenue for tuning the thermal energy distribution between the reforming/gasification and regeneration/decarbonation steps, thereby minimizing the exergy loss for hydrogen generation.

Taking advantage of the inherent flexibility of perovskite structures, we conducted a comprehensive screening of 1225 A/B-site doped perovskite oxides ($Sr_xA_{1-x}Fe_yB_{1-y}O_{3-\delta}$) using plane wave density functional theory (DFT) calculations of structures and free energies. The effectiveness of our redox-activated sorbent concept and the proposed computational framework was validated experimentally. The advanced sorbents developed in this research achieved high capacity and versatility for biomass gasification, biogas, and methane reforming. The use of concentrated O_2 in the regeneration step can facilitate integrated CO_2 capture, resulting in a life-cycle CO_2 emission as low as −2.18 kg CO_2-eq per kg of H_2.

2. Results and discussion

2.1. High throughput computational screening

In all, 1225 sorbent compositions, with a general formula of $Sr_xA_{1-x}Fe_yB_{1-y}O_{3-\delta}$ (A = Ca, K, or Ba and B = Mn, Ti, Co, Cu, Ni, or Mg), were considered in this study. The workflow for the computational screening is summarized in Fig. 2a. Initial steps in the workflow focus on ensuring the pre-requisites for the sorbent compositions, namely (i) charge neutrality and (ii) structural stability.

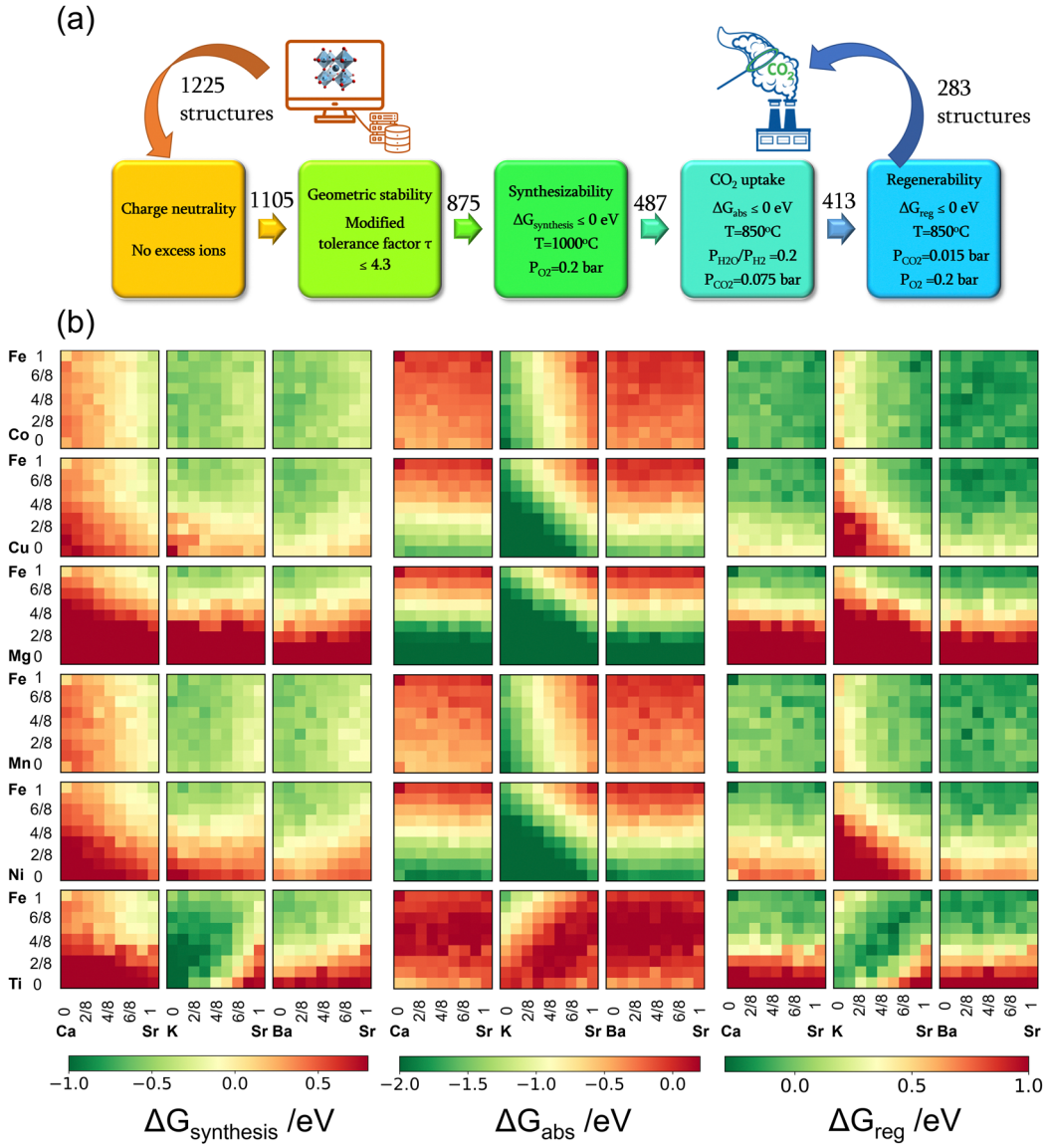

Fig. 2 Computational screening approach and results. (a) Screening workflow for iSERG sorbents. The values above each arrow represent the count of perovskite structures that successfully passed the preceding screening step. (b) Heatmaps of the thermodynamic descriptors of the 1225 candidates. The values of the x and y axes denote the concentrations of Sr and Fe in $Sr_xA_{1-x}Fe_yB_{1-y}O_{3-\delta}$, respectively.

Firstly, the charge neutrality of various A and B-site cation combinations in the $Sr_xA_{1-x}Fe_yB_{1-y}O_{3-\delta}$ structures were assessed. The total positive charge of all cations must be able to balance the total negative charge of all anions (*i.e.*, O^{2-}).[40] Out of the initial set, 120 compositions failing to satisfy the charge neutrality criterion were excluded from further consideration, with most of these containing a large fraction of Mg ($\geq$50%). Subsequently, the structural stability of the remaining perovskite compositions was investigated using the modified tolerance factor (τ) proposed by Bartel *et al.*[41] Derived from extensive data sets, this descriptor has demonstrated superior predictive capability for perovskite stability compared to the geometric-based Goldschmidt tolerance factor. A relaxed criterion of $\tau < 4.3$, as reported in our recent work,[40] was used to screen out 230 compositions that are likely to be unstable in a perovskite structure. Many of them contained a large fraction of K on the A-site and were shown to be unstable based on our previous synthesis experience. These screening steps narrowed down the sorbent candidates to 875 compositions, summarized in Fig. S1(a) (see ESI†).

Beyond structural stability, a suitable perovskite sorbent for isothermal SERG must satisfy the following criteria:

(i) Synthesizability: the mixed oxide should be more stable than a simple mixture of its monometallic oxide precursors in an oxidizing environment (*e.g.*, air);

(ii) Sorption capability: the sorbent should undergo spontaneous reduction and carbonation under a reducing environment and in the presence of CO_2;

(iii) Regenerability: the sorbent should spontaneously release CO_2 and reform the $ABO_{3-\delta}$ structure under an oxidizing environment.

The reactions corresponding to these criteria are listed below. Given the reducing atmosphere in the gasifier/reformer, a Brownmillerite phase with a general formula of $ABO_{2.5}$ was considered in these reactions. Operational parameters compatible with actual operating conditions were used as the input parameters for the analysis. For instance, the synthesis condition was set at 1000 °C and P_{O_2} = 0.2 bar. The sorption step condition was 850 °C with P_{H_2O}/P_{H_2} = 0.2 and P_{CO_2} = 0.075 bar. The regeneration step condition was P_{O_2} = 0.2 bar and P_{CO_2} = 0.015 bar. We also note that these sorbent particles absorb CO_2 *via* a carbonation reaction. Therefore, the sorbents are chemically specific for CO_2 absorption and does not adsorb or absorb H_2, N_2, or CH_4.

$$x\mathrm{SrO} + \frac{1-x}{m}\mathrm{A}_m\mathrm{O}_n + \frac{y}{2}\mathrm{Fe}_2\mathrm{O}_3 + \frac{1-y}{i}\mathrm{B}_i\mathrm{O}_j + z_1\mathrm{O}_2 \rightarrow \mathrm{Sr}_x\mathrm{A}_{1-x}\mathrm{Fe}_y\mathrm{B}_{1-y}\mathrm{O}_{2.5} \quad (1)$$

$$\mathrm{Sr}_x\mathrm{A}_{1-x}\mathrm{Fe}_y\mathrm{B}_{1-y}\mathrm{O}_{2.5} + \mathrm{CO}_2 + z_2\mathrm{H}_2 \rightarrow x\mathrm{SrCO}_3 + \frac{1-x}{m}\mathrm{A}_m\mathrm{CO}_3 + \frac{y}{2}\mathrm{Fe}_2\mathrm{O}_3 + \frac{1-y}{i}\mathrm{B}_i\mathrm{O}_j + z_2\mathrm{H}_2\mathrm{O} \quad (2)$$

$$x\mathrm{SrCO}_3 + \frac{1-x}{m}\mathrm{A}_m\mathrm{CO}_3 + \frac{y}{2}\mathrm{Fe}_2\mathrm{O}_3 + \frac{1-y}{i}\mathrm{B}_i\mathrm{O}_j + z_3\mathrm{O}_2 \rightarrow \mathrm{Sr}_x\mathrm{A}_{1-x}\mathrm{Fe}_y\mathrm{B}_{1-y}\mathrm{O}_{2.5} + \mathrm{CO}_2 \quad (3)$$

The Gibbs free energies of reactions (1)–(3), denoted as $\Delta G_{\mathrm{syn(thesis)}}$, $\Delta G_{\mathrm{abs(orption)}}$, and $\Delta G_{\mathrm{reg(eneration)}}$, respectively, are delineated in Fig. 2b for the 875 compositions under examination. To meet the screening criteria, these ΔGs should be ≤ 0 eV to ensure adequate thermodynamic driving forces. Applying this criterion, 283 compositions were identified as potentially suitable candidates for isothermal SERG operations. Computational details, based on a combination of DFT calculations of the perovskite oxides and the bulk thermodynamic properties of both the monometallic oxides and carbonates, are provided in the methodology section. Table 1 highlights several promising sorbent composition families, whereas Fig. S1e (see ESI†) summarizes all the suitable candidates predicted by the simulation. It is noted that over 90% of the SrBaFeCo and SrBaFeMn compositions were predicted to be favorable for iSERG. Therefore, our experimental investigation prioritized the SrBaFeCo and SrBaFeMn families of sorbents.

Table 1 Promising composition families and the corresponding dopant concentration ranges predicted by computational screening

Compositions	General dopant concentrations at A-site and B-site
SrBaFeMn	Ba: 0–1; Mn: 0–1
SrBaFeCo	Ba: 0–1; Co: 0–1
SrBaFeCu	Ba: 0–1; Cu: 0–0.5
SrCaFeCo	Ca: 0–0.375; Co: 0–1
SrBaFeNi	Ba: 0–1; Ni: 0–0.375

2.2. Experimental evaluation of sorbent isothermal performance

To assess the computational screening results, 100 sorbent compositions were prepared and characterized. Among these, 80 were deemed thermodynamically suitable for iSERG applications based on the computation results. As depicted in Fig. 3a and detailed in Table S1 and Fig. S2 (see ESI†), X-ray diffraction (XRD) analyses revealed that 72 of the samples contained a single perovskite phase, while an additional 13 displayed minimal phase impurities. The remaining 15 samples presented at least one prominent secondary phase, although perovskite phase(s) were observed in all the samples. This confirms the effectiveness of computational screening in predicting the stability and synthesizability of the perovskite sorbents. Notably, most cobalt-containing materials, *i.e.*, $\mathrm{Sr}_x\mathrm{A}_{1-x}\mathrm{Fe}_y\mathrm{Co}_{1-y}\mathrm{O}_{3-\delta}$, were phase-pure. This may have resulted from the flexible valence states of Co and Fe as well as the similarities in ionic radii. On the other hand, Mn-doped materials tended to segregate into two distinct perovskite phases. Ni, Mg, and Cu-containing samples also tend to phase segregate when the doping level surpassed 12.5% (1/8) on the B-site, due to their instability at a valence state above 2+. It is noted that our model estimates phase stability and synthesizability based on the relative stability of perovskite and respective monometallic oxides (reaction (1)), it does not preclude the formation of alternative, more stable mixed oxide phases.

Fig. 2b displays the isothermal sorption capacities of the screened materials, defined as the percentage of A-site cations being reversibly carbonated, determined by thermogravimetric analysis (TGA). A relatively high operating temperature of 850 °C is chosen since it is commensurate with typical methane reforming and biomass gasification temperatures. This choice of operating temperature underscores an additional distinguishing feature of the redox-activated iSERG sorbents: whereas conventional sorbents are ineffective for CO_2 sorption at >700 °C due to thermodynamic constraints, the iSERG sorbents do not face this limitation. This thermodynamic flexibility allows them to maintain effectiveness in the conversion of biomass and biogas. In terms of sorbent performance, it was observed that calcium doping in the A-site reduced the CO_2 capacity, while barium doping resulted in an increase. This trend can be explained by the instability of $CaCO_3$ at 850 °C, whereas $BaCO_3$ exhibits better stability than $SrCO_3$. Additionally, all samples with <25% B-site doping exhibited low sorption capacity, indicating that the B-site cation composition also plays a critical role in sorbent performance. This observation lends further credence to the proposed iSERG concept (Fig. 1), emphasizing the link between the redox behavior of the B-site cations and the carbonation and decarbonation reactions. For instance, $SrFeO_{3-\delta}$ showed a negligible (~0.13%) CO_2 sorption capacity, but upon doping the B-site with 75% Mn, the CO_2 capacity increased to 21%. Further increasing the Mn fraction to 87.5% boosted the CO_2 capacity to 59%. This finding aligns with DFT simulations, which revealed a decrease in ΔG_{abs} of 0.3 eV as Mn doping increased from 12.5% to 87.5%. More detailed fitting results (see ESI:† Fig. S3(a–c)) unveiled robust

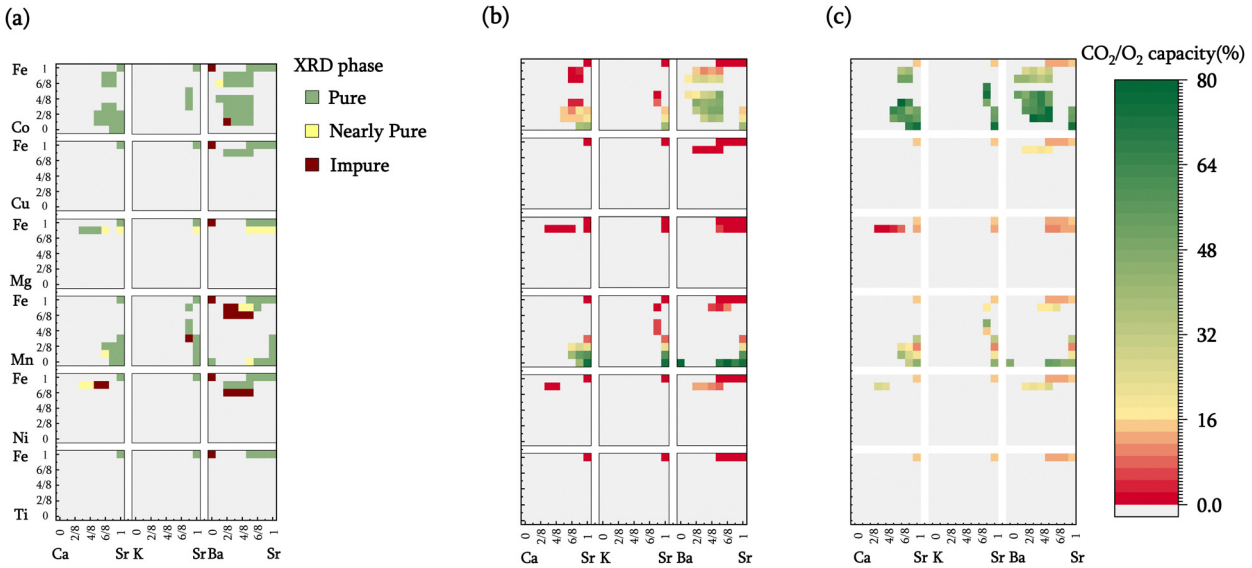

Fig. 3 Experimental evaluation of the sorbents. (a) Phase purity of the synthesized perovskites: green-, yellow- and burgundy-colored cells represent pure, nearly pure, and impure samples, respectively. (b) CO_2 sorption capacities and (c) oxygen capacities of pure and nearly pure materials measured in the TGA. The rightmost color bar represents the CO_2 capacity for (b) and the O_2 capacity for (c).

correlations (R^2 between 0.7–0.9) between the dopant fractions of A-site and B-site elements and the CO_2 capacity. Additionally, doping the B-site with Ni, Mg, and Cu in amounts greater than 12.5% leads to phase segregation and are thus not suitable for iSERG.

Of all the samples tested, 21 perovskite oxides exhibited excellent sorption capacities (>35%). These high-performing sorbents primarily belong to three families: $Sr_xBa_{1-x}Fe_yCo_{1-y}O_{3-\delta}$, $Sr_xCa_{1-x}Fe_yMn_{1-y}O_{3-\delta}$, and $Sr_xBa_{1-x}Fe_yMn_{1-y}O_{3-\delta}$. Among these, $Sr_{0.75}Ba_{0.25}MnO_{3-\delta}$ registered the highest CO_2 capacity of 78%, closely followed by $BaMnO_{3-\delta}$ and $SrMnO_{3-\delta}$ with capacities of 77% and 75%, respectively. Within the tested $Sr_xBa_{1-x}Fe_yCo_{1-y}O_{3-\delta}$ samples, $Sr_{0.625}Ba_{0.375}Fe_{0.5}Co_{0.5}O_{3-\delta}$ displayed the highest CO_2 capacity of ~49%. Additionally, $SrFeO_{3-\delta}$ samples with elevated levels of cobalt doping also exhibited significant sorption capacities, such as $SrCoO_{3-\delta}$, which had a CO_2 capacity of 40%. However, the cost of cobalt may limit their economic attractiveness.

In addition to the sorption capacity, the redox-based oxygen capacity, defined as the percentage of reducible lattice oxygen removed during the gasification/reforming step, is an important parameter for redox-activated sorbents. The oxygen capacity influences (i) the overall heat of reaction for the two-step process, as the redox reaction facilitates *in situ* combustion of a fraction of the feedstock to counterbalance the endothermic gasification or reforming processes; and (ii) the distribution of reaction heat between the two steps. Specifically, the exothermic oxidation reaction would partially offset the heat required for carbonate decomposition, while the endothermic reduction reaction mitigates heat release during the carbonation reaction. Oxygen capacities for the screened materials are depicted in Fig. 3c.

Generally, within a specific sorbent family (*e.g.*, $Sr_xBa_{1-x}Fe_yCo_{1-y}O_{3-\delta}$), compositions exhibiting higher sorption capacities also tend to have higher oxygen capacities. This relationship suggests a positive correlation between the carbonation and reduction reactions, aligning with the proposed iSERG concept. Oxygen capacities are also greatly influenced by both the type and levels of dopants at the B site. For instance, materials doped with cobalt generally exhibit greater oxygen capacity than other dopants. Increasing the B-site dopant level also significantly enhanced the oxygen capacities and reducibility of the sorbents. These distinctive characteristics provide us a broad design space for choosing redox-activated CO_2 sorbents, allowing for the design of materials that optimally balance CO_2 sorption and redox properties, thereby improving iSERG performance.

2.3. Correlating computational results and experimental performance

Although our screening method primarily focused on evaluating the thermodynamic feasibility and driving forces associated with sorption–desorption reactions, it is nevertheless instructive to explore the correlations between experimentally measured sorption capacities and the reaction free energies predicted by DFT. Fig. 4a depicts the relationships between CO_2 sorption capacity and various ΔGs for the 85 samples that are either pure or nearly phase-pure. Meanwhile, Fig. 4b presents a confusion matrix and highlights the key parameters of the matrix to underscore the model's accuracy. Considering the potential experimental errors that can arise during CO_2 capacity measurement, we adopted 2% sorbent capacity as a threshold for determining thermodynamic feasibility for iSERG applications. As can be seen, the screening model achieved a precision rate of 80% and an F1 score of 0.82, confirming the effectiveness of our model and the screening criteria.

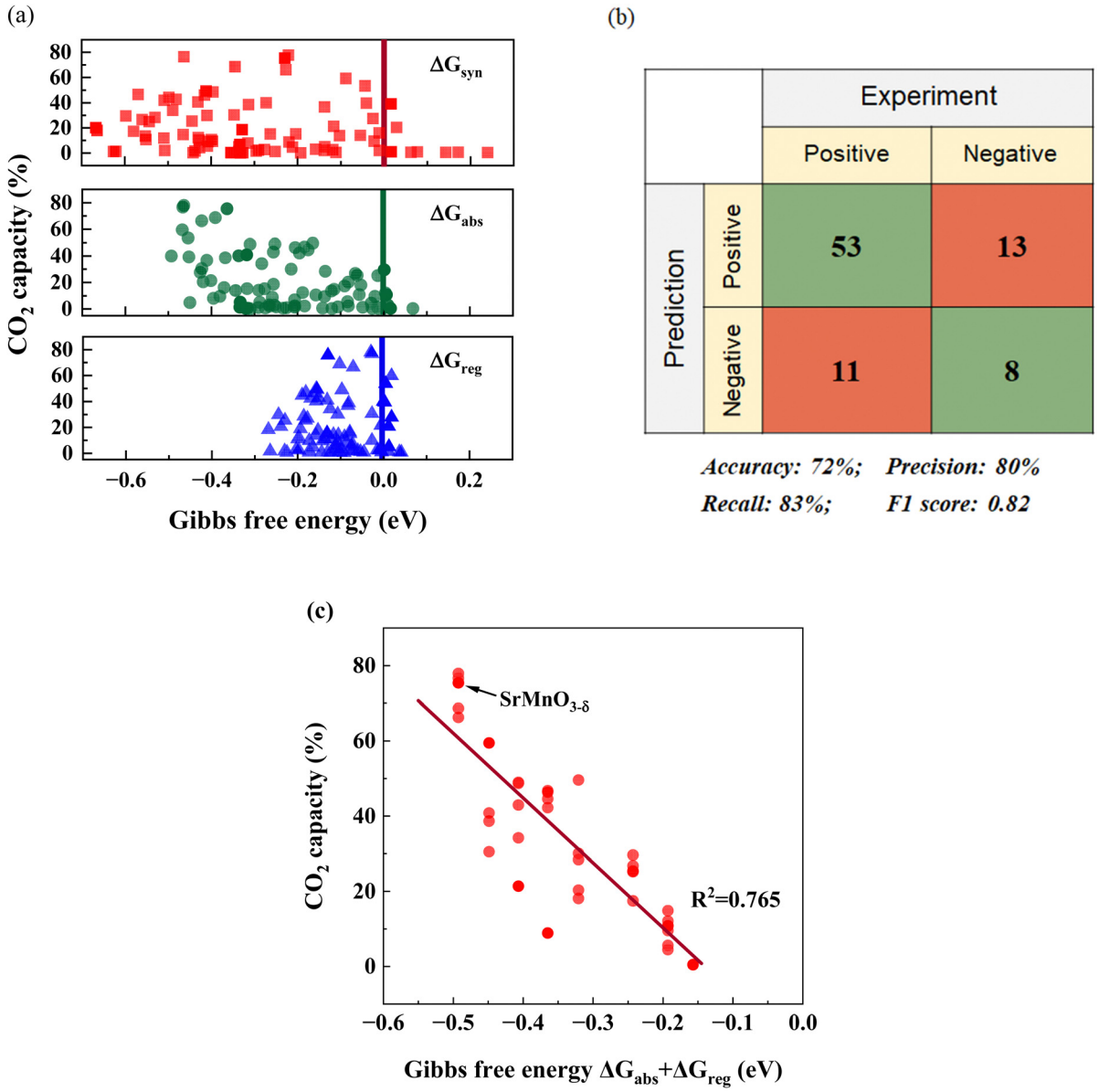

Fig. 4 Correlation between computational and experimental results. (a) Relationships between the CO_2 capacity and the different computed ΔGs. (b) Confusion matrix and the performance of the screening model. A sample is classified as "Positive" if it exhibits a CO_2 capacity greater than 2%, since this confirms thermodynamic feasibility. Conversely, it is labeled as "Negative" if the capacity is less than 2%. For the prediction aspect, a "Positive" classification indicates the candidate meets all the criteria in Fig. 2a and otherwise it is classified as "Negative". (c) Correlation between the CO_2 capacity and ΔG_{abs} + ΔG_{reg} for $Sr_xBa_{1-x}Fe_yB_{1-y}O_{3-\delta}$ (B = Co/Mn) perovskites (40 materials total).

While predicting a sorbent's thermodynamic feasibility is crucial, identifying an effective descriptor for CO_2 capacity holds greater practical value. It is therefore informative to investigate the correlation between the computationally derived thermodynamic parameters and the experimentally derived sorbent capacity. We note that ΔG_{syn}, ΔG_{abs}, or ΔG_{reg}, when used as a single fitting parameter, exhibited a weak correlation to CO_2 capacity. Given the tendency for $CaCO_3$ to decompose at the temperature of interest (850 °C) and the uncertainty related to Ca-containing solid solutions, the following fitting focused on the $Sr_xBa_{1-x}Fe_yB_{1-y}O_{3-\delta}$ (B = Co/Mn) based materials (40 in total). Among all the fitting correlations, which are detailed in Table S2 (ESI†), the one involving (ΔG_{abs} + ΔG_{reg}) displayed a relatively strong relationship with CO_2 capacity, exhibiting a statistical R^2 value of 0.765. We also note that multiple regressions provided similar correlations (Table S2, ESI†). As a descriptor, (ΔG_{abs} + ΔG_{reg}) also holds physical significance: materials that exhibit low (ΔG_{abs} + ΔG_{reg}), which correspond to higher overall thermodynamic favorability for the carbonation and decarbonation steps tend to exhibit higher sorption capacities. This concise descriptor can notably improve the effectiveness for sorbent optimization, since it strikes a good balance among efficiency, accuracy, and practicality. Although the current model does not consider kinetic parameters, the

sorption and regeneration rates are both sufficient for efficient reforming/gasification and fast regeneration, as demonstrated in the next section.

2.4. Demonstration of isothermal hydrogen generation

Considering its simplicity, lower raw material cost, and relative ease of scalable synthesis, we selected $SrMnO_{3-\delta}$ for comprehensive performance evaluations. As shown in Fig. 5a, $SrMnO_3$ is highly effective for iSERG of various carbonaceous feedstocks, producing ~95% pure H_2 from both biogas and methane, and yielding hydrogen enriched syngas with 73 vol% H_2 from biomass under its more selective regime. Fig. 5b shows the sorbent stability under repeated iSERG cycles using simulated biogas ($CH_4:CO_2$ = 2:1). The XRD of reduced and regenerated samples also affirmed the reversible phase transitions (Fig. S4, ESI†). Detailed data for the $SrMnO_{3-\delta}$ sorbent with respect to the typical product gas profiles and cyclic stability with methane, biogas, and biomass are summarized in Fig. S5 (see ESI†). We note that during the initial stage of the reaction, the $SrMnO_{3-\delta}$ sorbent tends to be less selective. This is likely related to the less selective oxygen species associated with the high initial oxidation state of Mn in $SrMnO_{3-\delta}$. In fact, a pre-reduction of the sorbent can substantially improve selectivity (Fig. S5(h), ESI†). Following a transition to $SrMnO_{2.5}$, concentrated hydrogen with low CO_2 concentration was produced. As depicted in Fig. S5(a/b) (see ESI†), even with a small sorbent bed containing 1.5 g of sorbent particles, the hydrogen production stage from methane was longer than 10 minutes, with ~95% H_2 purity before the CO_2 breakthrough. The presence of CO_2 in biogas accelerates the saturation of the sorbent, leading to a shorter yet still significant pre-breakthrough period (>5 min) for hydrogen

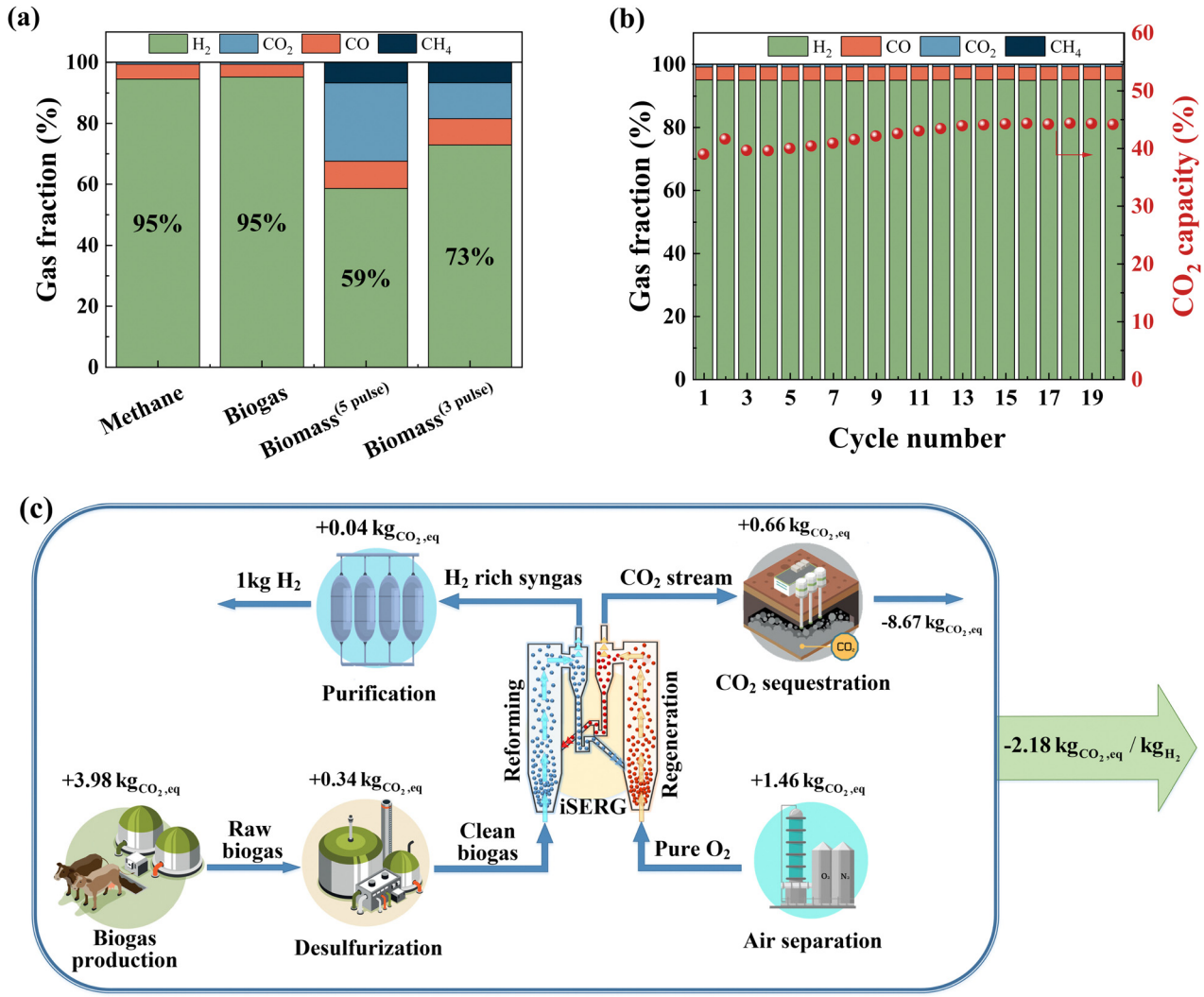

Fig. 5 iSERG with a $SrMnO_3$ sorbent. (a) Product gas compositions from iSERG using methane, biogas ($CH_4:CO_2$ = 2:1), and biomass feedstocks. Biomass$^{(5pulse)}$ represents the average gas composition of five consecutive injections of biomass samples into the fluidized bed whereas Biomass$^{(3pulse)}$ represents the average gas composition from the last three injections, *i.e.*, the more selective regime. (b) Cyclic stability of the sorbent over 20 cycles using simulated biogas ($CH_4:CO_2$ = 2:1). Gas fraction is shown in a dry and Ar-free basis during the low-CO_2 period. (c) Schematic of the life-cycle analysis (LCA) for hydrogen production *via* the iSERG process. The global warming potential (GWP) was calculated based on a per kg H_2 basis. Recycle of the tail gas from the hydrogen purification step is not shown in this simplified schematic.

production with ~95% purity (Fig. S5(c/d), ESI†). The sorbent also exhibited promising performance for biomass gasification in a fluidized bed reactor (Fig. S5(e–g), ESI†). Again, the initial stage for $SrMnO_3$ reduction was accompanied by CO_2 generation. This is followed by high selectivity for hydrogen generation with effective *in situ* CO_2 removal.

An additional attractive feature of the iSERG is its capability for integrated CO_2 capture. By modulating the duration of the regeneration step with the $SrMnO_3$ sorbent, pure CO_2 can be produced without a breakthrough of O_2 (Fig. S5(i/j), ESI†). For practical implementation in a circulating fluidized bed based iSERG gasifier, we anticipate a better control over the degree of regeneration of the sorbent particles to further decrease CO_2 selectivity in the gasification step while producing concentrated CO_2 in the regeneration step. The latter is accomplished using concentrated oxygen from an air separation unit as the oxidant. This will eliminate the need for the energy-intensive CO_2 separation step. Sequestering the captured carbon yields a carbon-negative hydrogen product with a life-cycle global warming potential (GWP) of −2.18 kg CO_2eq per kg H_2 (Fig. 5c and Table S3, ESI†).

3. Conclusions

This study reports a new approach that integrates both simulation and experimental methods to engineer a unique class of perovskite-structured, redox-activated CO_2 sorbents. These sorbents are characterized by their stable isothermal operation and adjustable heats of reactions, enabling an efficient isothermal sorption-enhanced reforming and gasification (iSERG) process for green hydrogen production. Specifically, a high-throughput computational screening of 1225 A/B-site doped $SrFeO_{3-\delta}$ was conducted using first-principles calculations to assess their structural stability and thermodynamic favorability for iSERG. Complementary to the simulation efforts, extensive experiments were carried out to validate the effectiveness of the computation-guided sorbent design framework. Out of the 100 sorbent candidates synthesized, 85 displayed predominantly pure perovskite phases. Moreover, 80% perovskite phases predicted to be active exhibited at least 2% CO_2 sorption capacities. Among these, $Sr_{0.75}Ba_{0.25}MnO_{3-\delta}$ demonstrated the highest CO_2 capacity of 78%, followed by $BaMnO_{3-\delta}$ of 77% and $SrMnO_{3-\delta}$ of 75%. An effective thermodynamic descriptor, $\Delta G_{abs} + \Delta G_{reg}$, was also identified, displaying strong correlation with the CO_2 capacity of sorbents. Finally, the $SrMnO_{3-\delta}$ sorbent was extensively demonstrated for hydrogen generation through sorption-enhanced steam reforming of methane and biogas, as well as sorption-enhanced gasification of biomass. Biomass gasification in a lab-scale fluidized bed yielded nearly 73% pure H_2, while both methane and biogas produced approximately 95% pure H_2. This reinforces the versatility and effectiveness of the iSERG sorbents developed in this study. Our findings also support the feasibility of integrating CO_2 capture in iSERG to yield carbon-negative hydrogen products from biogas with a life-cycle global warming potential as low as −2.18 kg CO_2eq per kg H_2.

4. Experimental section

4.1. DFT calculations

Density functional theory (DFT) calculations were conducted using VASP software.[42–45] The projector-augmented wave (PAW) method was used to calculate the interaction between electrons and atomic cores.[46,47] The generalized gradient approximation (GGA) approach[48] combined with the PBE exchange–correlation functional was applied to calculate the electronic structure and corresponding energies. The cutoff energy was 450 eV. The energy threshold was set to 10^{-5} eV and the force threshold to 0.01 eV $Å^{-1}$. Here spin polarization effect was considered with the initial spin moments of Co, Fe, Mn and Ni to be 5, 4, 4 and 5, respectively. In addition, and the DFT+*U* method was utilized to give accurate description of the d electrons for Co, Cu, Fe, Mn, Ni and Ti with the effective Hubbard *U* values of 3.4, 4, 4, 3.9, 6 and 3 (unit in eV).[49,50]

All the $2 \times 2 \times 1$ supercell structures were built based on the brownmillerite $SrFeO_{2.5}$ structure. We used the Monte Carlo quasi-random structures (MCSQS) algorithm implemented in the Alloy Theoretic Automated Toolkit (ATAT) code to generate the structures under different doping conditions.[51] We consider the A-site dopant elements: Ba, Ca, and K, and the B-site dopant elements: Co, Cu, Fe, Mn, Ni, and Ti. It is noted that our previous work considered other A-site metals such as La, Sm, and Y. However, their carbonates are unstable at the reaction temperature of interest. These A-site elements are probably unsuitable for CO_2 capture under high-temperature conditions, and they are not considered in this study. For A-site and B-site doping, the doping concentrations vary from 0 to 1 with an interval of 0.125, *i.e.*, $Sr_xA_{1-x}Fe_yB_{1-y}O_{2.5}$ with x and y to be 0, 0.125, …, 0.875, and 1. By following the SQS structure generation algorithm,[51] 1225 $Sr_xA_{1-x}Fe_yB_{1-y}O_{2.5}$ structures were obtained. In addition, we further conducted vibrational calculations for each structure and analyzed the results by using Phonopy, which could be further used to obtain free energies.[52,53] Similarly, calculations were performed on the metal oxides by the same procedures. Due to the complex spin state of O_2, its free energies were obtained by using the CBS-QB3 method implemented in Gaussian16,[54] and the energies were reported before.[40] The other gas phase species, such as CO_2, and H_2O, were calculated in a cubic box with a length of 10 Å.

4.2. Thermodynamic calculations

A reaction generator was developed to balance the reaction stoichiometry for the eqn (1)–(3). The Gibbs free energies of the perovskite structures and other relevant species are obtained using the methods in Section 4.1. The transition between the perovskite phase and the brownmillerite phase is spontaneous under the reduction and oxidation conditions. Therefore, the brownmillerite structure was chosen as the initial state of eqn (2) and the end state of eqn (3) in thermodynamic analysis. This calculation approach is expected to provide more accurate results compared to using perovskites. To minimize the error arising from the inaccurate description of the free energies of species such as carbonates, experimental Gibbs free energies

from HSC Chemistry software were utilized for solid reactions. These reactions include carbonation reactions (*e.g.*, SrO + CO_2 → $SrCO_3$) for eqn (2), decarbonation reactions for eqn (3), and hydrogen reduction to water for eqn (2). The reaction free energy $\Delta G \leq 0$ eV was used as the initial criteria for eqn (1)–(3). The energies of oxides, oxygen, *etc.* are from DFT VASP calculations.

The first thermodynamic screening step was aligned with typical perovskite synthesis conditions (1000 °C and P_{O_2} = 0.2 bar). Fig. 2b presents the heatmap displaying the ΔG_{syn} of all the structures. Notably, the stability of perovskites decreases with the increase in the doping concentrations of Cu, Mg, Ni, and Ti. However, this trend is not observed in samples doped with Co and Mn, making them more suitable for the SERG process due to their stability. A typical SERG temperature of 850 °C was selected as the reaction temperature of eqn (2) and (3). During the reduction/carbonation step, it is assumed that the system reaches equilibrium, with the partial pressure ratio P_{H_2O}/P_{H_2} set at 0.2 and P_{CO_2} at 0.075 bar. During the regeneration step, the obtained mixed metal oxides and carbonates are expected to regenerate under oxidation conditions with P_{O_2} = 0.2 bar and P_{CO_2} = 0.015 bar.

4.3. Sample synthesis and characterization

The perovskite materials for both the screening and reactor experiments were prepared using a solid-state reaction method. For a typical synthesis of $Sr_xCa_{1-x}Fe_yCo_{1-y}O_{3-\delta}$ for the screening experiment in the thermogravimetric analyzer (TGA), stoichiometric amounts of $SrCO_3$, $CaCO_3$, Fe_2O_3, and Co_3O_4 were added in a 5 mL Teflon vial and then mixed with 2 mm yttrium-stabilized ZrO_2 balls with a mass ratio of 1 : 5. 2–3 mL ethanol (Fisher Scientific, CDA 19 (Histological)) was further added to the mixture to promote the mixing performance and reduce the particle size. A stainless-steel sample jar holding four vials with four different materials was balled milled at 1200 rpm for 3 h or 24 h using a high-energy ball mill (Vivtek Instrument: VBM-V80). The resulting wet slurry was dried in an oven at 95 °C for 30 min and 130 °C for another 30 min to remove ethanol. The dried powders were separated from ZrO_2 beads and then calcined at 1000 °C in a muffle furnace for 10 h to form the perovskite structure. The ramping rates for both heating and cooling steps were all set to 3 °C min^{-1}. Several Mn-doped materials were subjected to calcination at 1200 °C in a tube furnace to improve the phase purity. The fresh perovskite sorbents were sieved to two desired particle size ranges, *i.e.*, 180–250 μm for TGA experiments and 0–180 μm for XRD. A total of 100 different materials were synthesized for the screening experiments in the TGA. A large batch of $SrMnO_3$ was prepared for the reactor experiments. The precursors were mixed in two 150 mL and two 100 mL Teflon jars and ball-milled with 3 mm, 6 mm, and 10 mm ZrO balls and then milled at 250 rpm at a 45° angle for 12 h in a planetary ball mill (Columbia International, CIT-XBM4X-2.0L). The mixture of precursor powders after the drying step was first pelletized at 20 tons before calcined at 1100 °C in the muffle furnace. Afterwards, the resulting sorbent particles were sieved into a size of 180–425 μm. The rest of the synthesis procedures were the same as the screening study.

The precursors used in this study were $SrCO_3$ (Sigma Aldrich, >99.9%), $CaCO_3$ (Sigma Aldrich, >99%), BaO (Thermo Scientific, >99.5%), Co_3O_4 (Aldrich, >99%), Fe_2O_3 (Noah Chemicals, >99.9%), MnO_2 (Materion, >99.9%), CuO (Noah Chemicals, >99%), KNO_3 (Noah Chemicals, >99%), NiO (Noah Chemicals, >99%), and MgO (Materion, >99.5%). The phase structures of the prepared fresh sorbents were characterized on a PANalytical X'Pert PRO X-ray diffraction (XRD) operating at 45 kV and 40 mA. The sample was scanned from 2θ of 15° to 80° with a step size of 0.0262° and a hold time of 0.2 s for each step. The analyses and identifications of the XRD phases of all the samples were accomplished using High-score Plus software.

4.4. Experimental reactivity evaluation

4.4.1. TGA preliminary screening for the CO_2/O_2 capacity. The sorption capacities of the pure and almost pure sorbents were measured in two TGAs (TA SDT Q650 and TA SDT Q600). As illustrated in Fig. S7 (see ESI†), to replicate the sorption-enhanced process of carbonaceous fuels, a 4-step cycle configuration was employed, consisting of a reduction step, a regeneration step, and two purge steps before each half-cycle. During the experiments, approximately 30–50 mg of the fresh sorbents with a particle size of 180–250 μm were loaded into the TGA and then heated to 850 °C at a ramping rate of 30 °C min^{-1} under a flow of 140 sccm Ar (Airgas UHP 5.0 grade). The gas flow rates were controlled using Alicat mass flow controllers (MC-series). Once the temperature reached 850 °C, the furnace was purged with Ar for 8 min to ensure a stable reaction temperature. Subsequently, an additional flow of 40 sccm H_2 (Airgas UHP 5.0 grade) and 20 sccm CO_2 (Airgas 4.0 grade) was injected for 30 min. The perovskite sorbents underwent reduction and captured CO_2, leading to a noticeable weight gain. The H_2 and CO_2 gas flows were then stopped, and the furnace was purged with pure Ar for 8 min. Some of the carbonates decomposed during this step. In the subsequent 20 min regeneration step, an additional 35 sccm O_2 was injected. The reduced samples were initially re-oxidized and gained some weight in the first 1–2 min, followed by the release of a significant amount of CO_2. Afterward, the first cycle was accomplished, and an identical second cycle was initiated. The CO_2 capacity was determined by measuring the weight changes in the second cycle. However, certain perovskites exhibited limited kinetics, preventing complete regeneration within the 20 min time-frame. In order to ascertain the oxygen non-stoichiometry at the complete oxidation conditions, these perovskite materials were subjected to 850 °C under 20% O_2 atmosphere. Additionally, a reference point was established for each material by reducing the perovskite at 1100 °C in a 20% H_2 atmosphere, leading to a complete transformation to a mixture of pure metals and metal oxides. The CO_2 capacity was defined as the measured molar amount of CO_2 absorbed compared to the theoretical molar amount of CO_2 absorbed by A-site elements. The O_2 capacity was defined as the measured molar amount of

released O atoms compared to the molar amount of the sorbent. Further details about the calculation approach can be found in the ESI.†

4.4.2. Sorption-enhanced steam reforming of methane and biogas in a packed bed. The sorption-enhanced steam reforming of methane and biogas was demonstrated in a quartz U-tube-packed bed with a 6 mm inner diameter. As illustrated in Fig. S8 (see ESI†), a sequential bed configuration was utilized to achieve a high methane conversion. 0.3 g of nickel-based steam reforming catalysts (Alfa Aesar, HiFUEL R110) was utilized in the upstream section, and 1.5 g of sorbents were employed in the downstream section. Both the catalyst and sorbent particles were sieved to a size range of 180 to 425 μm. Quartz wool and SiC were used as inert packing material to prevent blowout and preheat the inlet gas. The reactor was heated to 850 °C at a ramping rate of 30 °C min^{-1} and then sustained at 850 °C throughout the entire experiment. A typical 4-step cycle configuration was also adopted, *i.e.*, a 20 min purge step, a 20 min reduction step, another 10 min purge step, and a 20 min regeneration step. A flow of 30 sccm Ar (Airgas UHP 5.0 grade) was maintained as the carrying gas throughout the entire cycle. For the methane reforming scenario, a flow of 5 sccm CH_4 (Airgas UHP 5.0 grade) was introduced during the reduction step along with 7.35 μL min^{-1} of deionized water regulated by a syringe pump. This corresponded to a steam-to-carbon molar ratio of 2. For the biogas reforming scenario, a flow of 5 sccm CH_4 (Airgas UHP 5.0 grade) was cofed with 2.5 sccm CO_2 (Airgas UHP 4.5 grade) alongside the continuous infusion of 7.35 μL min^{-1} of deionized water. The water was injected 3 min prior to methane injection, ensuring a stable steam flow rate at the onset of the reduction step. During the regeneration step, 7.5 sccm of O_2 (Airgas extra dry grade) was injected to create a 20% O_2 atmosphere.

To mitigate the less selective regime, another experiment was implemented with the incorporation of a pre-reduction step. The sample was pre-reduced with a gas mixture of 6 sccm H_2 and 30 sccm Ar for 10 min, followed by an Ar purge prior to the normal reaction cycle. Additionally, another experiment aimed at producing pure CO_2 without O_2 breakthrough for sequential carbon capture involved a shortened regeneration time. To control the reaction environment, 1.75 g sorbents, 4 sccm of CH_4, 2.3 sccm of CO_2, 5.88 μL min^{-1} of deionized water, and an 8 min regeneration time were utilized. The methane-to-carbon dioxide ratio was adjusted to match a typical biogas composition in the literature.[55] Throughout these experiments, steam was condensed and separated downstream, and the remaining gaseous products were analyzed using an MKS Cirrus II quadrupole mass spectrometer (QMS). The reduced and regenerated samples from the biogas experiments were collected and tested using XRD to validate the reversibility for phase transition. Due to mass transfer limitations in the pack bed, the regenerated samples taken from the reactors were treated in TGA at 850 °C under a continuous flow of 40 sccm O_2 and 160 sccm Ar prior to XRD characterization.

4.4.3. Sorption-enhanced gasification of biomass in a fluidized bed. The performance of $SrMnO_3$ for sorption-enhanced gasification of biomass was demonstrated in a laboratory-scale bubbling fluidized bed reactor. As shown in Fig. S9 (see ESI†), a vertical 304# stainless steel tube with a 25.4 mm outer diameter (OD) and 23.6 mm inner diameter (ID) was used as the reactor. The reactor was housed in a tube furnace (MTI OTF-1200X-S-VT) with a heating zone of around 20 cm. The furnace thermocouple (S-type), located in the middle of the heating zone, serves as the reference for the reaction temperature. Prior to the experiment, the bottom of the reactor tube was loaded with 16 mesh Al_2O_3 to support the sorbents. Subsequently, 15 g $SrMnO_3$ was loaded into the reactor, corresponding to a static bed height of approximately 2 cm. A typical 4-step cycle configuration was adopted, comprising of a reduction step, a regeneration step, and a purge step between each half-cycle. 923 sccm Ar (Airgas, UHP 5.0) was injected during the reduction and purge steps, while a mixture of 683 sccm Ar/240 sccm O_2 was injected during the regeneration step. The gas flow rates were controlled by mass flow controllers (Brooks, 5850 E series). Water was injected through a 3.18 mm OD × 1.76 mm ID stainless steel tube inserted into the heating zone. The temperature in the heating zone greatly surpassed the boiling point of the water, thereby ensuring vaporization of water into steam. The volumetric flow rate of water, controlled by a syringe pump (Harvard Apparatus), was set to 0.21 mL min^{-1}, corresponding to 277 sccm and a steam-to-Ar molar ratio of 0.3. The product gas stream was heat-traced before flowing through a flask submerged in ice water to condense the steam in the effluent and tar (if present). The effluent gas stream was then sent to an MKS Cirrus II quadrupole mass spectrometer to determine the gas compositions. For biomass injection into the reactor, a 3.75 mm OD/3.35 mm ID stainless steel tube was used. The lower end of the tube was inserted into the center of the sorbent bed to enhance the mixing of sorbents and biomass. A pulse injection mode was employed, where ~0.3 g of pulverized pine wood (200 to 500 μm) was first loaded into the top part of the tube, and then around 3 mL helium gas at 25 PSIG pressure was utilized to carry the biomass powder into the reactor. A second gas injection was performed subsequently to prevent any residual biomass from being stuck in the tubing. Five pulse injections of biomass were conducted for each cycle, and four cycles were conducted to achieve a stable sorption-enhanced performance for syngas production. The ultimate and proximate analyses of the biomass feedstock are listed in Table S4 (ESI†). The CO_2 capacity was also defined as the measured molar amount of CO_2 released in the regeneration step compared to the theoretical molar amount of CO_2 absorbed by A-site elements. The cold gas efficiency was defined as the produced gas calorific value with respect to the low heating value of biomass.

Author contributions

Conceptualization, F. L.; methodology, R. C., K. Y., X. W., F. L.; investigation, R. C., K. Y., X. W., M. R., A.-S. B., E. G., A. P., L. B., W. T.; writing – original draft, R. C., K. Y.; writing – review &

editing, R. C., K. Y., X. W., L. B., W. T., P. W., F. L.; funding acquisition, F. L.; resources, F. L.; supervision, F. L.

Data availability

The data supporting the findings are available within the main text and ESI.† More detailed data can be made available upon request.

Conflicts of interest

The authors declare no conflict of interest.

Acknowledgements

This work was supported by the U.S. Department of Energy Office of Energy Efficiency & Renewable Energy (no. EE0008809) and the US National Science Foundation (CBET-1923468). We acknowledge the use of the Analytical Instrumentation Facility (AIF) at North Carolina State University, which is supported by the State of North Carolina and the National Science Foundation. We also acknowledge the computing resources provided by North Carolina State University High Performance Computing Services Core Facility (RRID:SCR_022168). We also thank Dr Fan Yang and Dr Yuan Yao (Yale University) for their suggestions with respect to the life-cycle analysis.

References

1 C. Acar and I. Dincer, *Int. J. Hydrogen Energy*, 2020, **45**(5), 3396–3406.
2 T. da Silva Veras, T. S. Mozer, D. da Costa Rubim Messeder dos Santos and A. da Silva César, *Int. J. Hydrogen Energy*, 2017, **42**(4), 2018–2033.
3 M. Yue, H. Lambert, E. Pahon, R. Roche, S. Jemei and D. Hissel, *Renewable Sustainable Energy Rev.*, 2021, **146**, 111180.
4 International Energy Agency, Global hydrogen review 2022, Paris, **https://www.iea.org/reports/global-hydrogen-review-2022**, (Access. May. 6th, 2024), 2022.
5 A. Zapantis, *Circular carbon economy series: blue hydrogen*., 2021, **https://www.globalccsinstitute.com/wp-content/uploads/2021/04/Circular-Carbon-Economy-series-Blue-Hydrogen.pdf**, (Access. May 6th, 2024).
6 N. Sazali, *Int. J. Hydrogen Energy*, 2020, **45**(38), 18753–18771.
7 F. Dawood, M. Anda and G. M. Shafiullah, *Int. J. Hydrogen Energy*, 2020, **45**(7), 3847–3869.
8 L. Cao, I. K. M. Yu, X. Xiong, D. C. W. Tsang, S. Zhang, J. H. Clark, C. Hu, Y. H. Ng, J. Shang and Y. S. Ok, *Environ. Res.*, 2020, **186**, 109547.
9 V. S. Sikarwar, M. Zhao, P. Clough, J. Yao, X. Zhong, M. Z. Memon, N. Shah, E. J. Anthony and P. S. Fennell, *Energy Environ. Sci.*, 2016, **9**(10), 2939–2977.
10 U.S. Department of Energy. DOE national clean hydrogen strategy and roadmap, Jun. 2023, **https://www.hydrogen.energy.gov/library/roadmaps-vision/clean-hydrogen-strategy-roadmap** (Access May 6th, 2024).
11 X. Zhao, H. Zhou, V. S. Sikarwar, M. Zhao, A.-H. A. Park, P. S. Fennell, L. Shen and L.-S. Fan, *Energy Environ. Sci.*, 2017, **10**(9), 1885–1910.
12 Y. Gao, J. Jiang, Y. Meng, F. Yan and A. Aihemaiti, *Energy Convers. Manage.*, 2018, **171**, 133–155.
13 T. Mendiara, F. García-Labiano, A. Abad, P. Gayán, L. F. de Diego, M. T. Izquierdo and J. Adánez, *Appl. Energy*, 2018, **232**, 657–684.
14 J. Andersson and J. Lundgren, *Appl. Energy*, 2014, **130**, 484–490.
15 Y. Richardson, J. Blin and A. Julbe, *Prog. Energy Combust. Sci.*, 2012, **38**(6), 765–781.
16 M. Puig-Gamero, J. Argudo-Santamaria, J. L. Valverde, P. Sánchez and L. Sanchez-Silva, *Energy Convers. Manage.*, 2018, **177**, 416–427.
17 A. M. Parvez, S. Hafner, M. Hornberger, M. Schmid and G. Scheffknecht, *Renewable Sustainable Energy Rev.*, 2021, **141**, 110756.
18 D. Chen and L. He, *ChemCatChem*, 2011, **3**(3), 490–511.
19 M. Broda, A. M. Kierzkowska, D. Baudouin, Q. Imtiaz, C. Copéret and C. R. Müller, *ACS Catal.*, 2012, **2**(8), 1635–1646.
20 C. Dang, L. Liu, G. Yang, W. Cai, J. Long and H. Yu, *Chem. Eng. J.*, 2020, **383**, 123204.
21 J. Udomsirichakorn, P. Basu, P. Abdul Salam and B. Acharya, *Fuel Process. Technol.*, 2014, **127**, 7–12.
22 H. An, T. Song, L. Shen, C. Qin, J. Yin and B. Feng, *Int. J. Hydrogen Energy*, 2012, **37**(19), 14195–14204.
23 B. Jiang, B. Dou, K. Wang, C. Zhang, M. Li, H. Chen and Y. Xu, *Chem. Eng. J.*, 2017, **313**, 207–216.
24 J. C. Abanades, *Chem. Eng. J.*, 2002, **90**(3), 303–306.
25 F. D. M. Daud, K. Vignesh, S. Sreekantan and A. R. Mohamed, *New J. Chem.*, 2016, **40**(1), 231–237.
26 G. S. Grasa and J. C. Abanades, *Ind. Eng. Chem. Res.*, 2006, **45**(26), 8846–8851.
27 V. Manovic and E. J. Anthony, *Environ. Sci. Technol.*, 2007, **41**(4), 1420–1425.
28 H. K. Rusten, E. Ochoa-Fernández, H. Lindborg, D. Chen and H. A. Jakobsen, *Ind. Eng. Chem. Res.*, 2007, **46**(25), 8729–8737.
29 H. R. Radfarnia and M. C. Iliuta, *Chem. Eng. Process.*, 2014, **86**, 96–103.
30 G. Wu, C. Zhang, S. Li, Z. Huang, S. Yan, S. Wang, X. Ma and J. Gong, *Energy Environ. Sci.*, 2012, **5**(10), 8942.
31 A. Armutlulu, M. A. Naeem, H. J. Liu, S. M. Kim, A. Kierzkowska, A. Fedorov and C. R. Muller, *Adv. Mater.*, 2017, **29**(41), 1702896.
32 M. T. Dunstan, F. Donat, A. H. Bork, C. P. Grey and C. R. Muller, *Chem. Rev.*, 2021, **121**(20), 12681–12745.
33 V. Manovic and E. J. Anthony, *Fuel*, 2011, **90**(1), 233–239.
34 F.-C. Yu, N. Phalak, Z. Sun and L.-S. Fan, *Ind. Eng. Chem. Res.*, 2011, **51**(4), 2133–2142.
35 H. Sun, J. Wang, J. Zhao, B. Shen, J. Shi, J. Huang and C. Wu, *Appl. Catal., B*, 2019, **244**, 63–75.

36 L. Brody, R. Cai, A. Thornton, J. Liu, H. Yu and F. Li, *ACS Sustainable Chem. Eng.*, 2022, **10**(19), 6434–6445.
37 C. Dang, Y. Li, S. M. Yusuf, Y. Cao, H. Wang, H. Yu, F. Peng and F. Li, *Energy Environ. Sci.*, 2018, **11**(3), 660–668.
38 C. Dang, H. Yu, H. Wang, F. Peng and Y. Yang, *Chem. Eng. J.*, 2016, **286**, 329–338.
39 L. Brody, M. Rukh, R. Cai, A. Saberi Bosari, R. Schomäcker and F. Li, *J. Phys. Energy*, 2023, **5**(3), 035004.
40 X. Wang, Y. Gao, E. Krzystowczyk, S. Iftikhar, J. Dou, R. Cai, H. Wang, C. Ruan, S. Ye and F. Li, *Energy Environ. Sci.*, 2022, **15**(4), 1512–1528.
41 C. J. Bartel, C. Sutton, B. R. Goldsmith, R. Ouyang, C. B. Musgrave, L. M. Ghiringhelli and M. Scheffler, *Sci. Adv.*, 2019, **5**(2), eaav0693.
42 G. Kresse and J. Furthmüller, *Comput. Mater. Sci.*, 1996, **6**(1), 15–50.
43 G. Kresse and J. Furthmuller, *Phys. Rev. B: Condens. Matter Mater. Phys.*, 1996, **54**(16), 11169–11186.
44 G. Kresse and J. Hafner, *Phys. Rev. B: Condens. Matter Mater. Phys.*, 1993, **47**(1), 558–561.
45 G. Kresse and J. Hafner, *Phys. Rev. B: Condens. Matter Mater. Phys.*, 1994, **49**(20), 14251–14269.
46 P. E. Blochl, *Phys. Rev. B: Condens. Matter Mater. Phys.*, 1994, **50**(24), 17953–17979.
47 G. Kresse and D. Joubert, *Phys. Rev. B: Condens. Matter Mater. Phys.*, 1999, **59**(3), 1758–1775.
48 J. P. Perdew, K. Burke and M. Ernzerhof, *Phys. Rev. Lett.*, 1996, **77**(18), 3865–3868.
49 A. Jain, G. Hautier, C. J. Moore, S. Ping Ong, C. C. Fischer, T. Mueller, K. A. Persson and G. Ceder, *Comput. Mater. Sci.*, 2011, **50**(8), 2295–2310.
50 G. Hautier, S. P. Ong, A. Jain, C. J. Moore and G. Ceder, *Phys. Rev. B: Condens. Matter Mater. Phys.*, 2012, **85**(15), 155208.
51 A. van de Walle, P. Tiwary, M. de Jong, D. L. Olmsted, M. Asta, A. Dick, D. Shin, Y. Wang, L. Q. Chen and Z. K. Liu, *CALPHAD: Comput. Coupling Phase Diagrams Thermochem.*, 2013, **42**, 13–18.
52 A. Togo, *J. Phys. Soc. Jpn.*, 2023, **92**(1), 012001.
53 A. Togo and I. Tanaka, *Scr. Mater.*, 2015, **108**, 1–5.
54 M. J. Frisch, G. W. Trucks, H. B. Schlegel, G. E. Scuseria, M. A. Robb, J. R. Cheeseman, G. Scalmani, V. Barone, G. A. Petersson, H. Nakatsuji, X. Li, M. Caricato, A. V. Marenich, J. Bloino, B. G. Janesko, R. Gomperts, B. Mennucci, H. P. Hratchian, J. V. Ortiz, A. F. Izmaylov, J. L. Sonnenberg, D. Williams-Young, F. Ding, F. Lipparini, F. Egidi, J. Goings, B. Peng, A. Petrone, T. Henderson, D. Ranasinghe, V. G. Zakrzewski, J. Gao, N. Rega, G. Zheng, W. Liang, M. Hada, M. Ehara, K. Toyota, R. Fukuda, J. Hasegawa, M. Ishida, T. Nakajima, Y. Honda, O. Kitao, H. Nakai, T. Vreven, K. Throssell, J. A. Montgomery Jr., J. E. Peralta, F. Ogliaro, M. J. Bearpark, J. J. Heyd, E. N. Brothers, K. N. Kudin, V. N. Staroverov, T. A. Keith, R. Kobayashi, J. Normand, K. Raghavachari, A. P. Rendell, J. C. Burant, S. S. Iyengar, J. Tomasi, M. Cossi, J. M. Millam, M. Klene, C. Adamo, R. Cammi, J. W. Ochterski, R. L. Martin, K. Morokuma, O. Farkas, J. B. Foresman and D. J. Fox, *Gaussian 16 Rev. C.01*, Gaussian Inc., Wallingford, CT, 2016.
55 N. Hajjaji, S. Martinez, E. Trably, J.-P. Steyer and A. Helias, *Int. J. Hydrogen Energy*, 2016, **41**(14), 6064–6075.

